CrossMark

TECHNICAL PAPER

The MEMS four-leaf clover wideband vibration energy harvesting device: design concept and experimental verification

J. Iannacci[1] · **G. Sordo**[1] · **E. Serra**[1] · **U. Schmid**[2]

Abstract In this contribution, we discuss a novel design concept of a high-performance wideband MEMS vibration energy harvester (EH), named four-leaf clover (FLC EH-MEMS) after its circular shape featuring four petal-like mass-spring systems. The goal is to enable multiple resonant modes in the typical range of vibrations scattered in the environment (i.e., up to 4–5 kHz). This boosts the FLC conversion capability from mechanical into electrical energy exploiting the piezoelectric effect, thus overcoming the common limitation of cantilever-like EHs that exhibit good performance only in a very narrow band of vibration (i.e., fundamental resonant mode). The FLC concept is first discussed framing it into the current state of the art, highlighting its strengths. Then, after a brief theoretical introduction on mechanical resonators, the FLC EH-MEMS device is described in details. Finite Element Method (FEM) analyses are conducted in the ANSYS Workbench™ framework. A suitable 3D model is built up to perform modal simulations, aimed to identify mechanical resonant modes, as well as harmonic analyses, devoted to study the mechanical and electrical behaviour of the FLC EH-MEMS (coupled field analysis). The work reports on experimental activities, as well. Physical samples of the FLC EH-MEMS device are fabricated within a technology platform that combines surface and bulk micromachining. Thereafter, specimens are tested both with a laser doppler vibrometer measurement setup as well as with a dedicated shaker-based setup, and the results are compared with simulations for validation purposes. In conclusion, the FLC EH-MEMS exhibits a large number of resonant modes scattered in the tested range of vibrations (up to 15 kHz) already starting from frequencies as low as 200 Hz, and expected levels of converted power better than 10 µW.

1 Introduction

We are living in a world where the surrounding environment and the objects supporting us in daily life are seamlessly becoming more adaptive and interconnected. Services are broader, more capillary, linked together and easy to access. Experiences are tailored to our preferences and specific (as well as special) needs. The attribute 'smart' is now frequently associated to diverse application fields of science and technology, giving rise to familiar keywords like Smart Cities, Smart Homes, Smart Objects, etc. (Vasseur and Dunkels 2010). Thereupon, the paradigm of the Internet of Things (IoT) appears to be the common denominator of all the listed applications, providing connectivity, interoperability and communication of smart entities (objects, environments, etc.) within a pervasive network (Uckelmann et al. 2011). In other words, IoT bears the seed to address the Societal Challenges of future population on worldwide basis (e.g., clean and efficient energy). Being established on networks of distributed sensors/actuators (i.e., wireless sensor networks—WSNs) (Dargie and Poellabauer 2010), IoT applications demand for smart, integrated, miniaturized and low-energy consumption wireless

✉ J. Iannacci
  iannacci@fbk.eu

1 MicroSystems Technology (MST) Research Unit, Center for Materials and Microsystems (CMM), Fondazione Bruno Kessler (FBK), Via Sommarive 18, 38123 Povo, Trento, Italy

2 Institute of Sensor and Actuator Systems (ISAS), Vienna University of Technology (VUT), Floragasse, 7, 1040 Vienna, Austria

Springer

nodes, typically powered by non-renewable energy storage units (i.e., batteries). The latter aspect poses relevant constraints as batteries have a limited lifetime and often their replacement is impracticable. On the other hand, the availability of zero-power energy-autonomous technologies, able to harvest (i.e., convert) and store part of the energy available in the surrounding environment (e.g., vibrations, thermal gradients and electromagnetic waves) into electricity to supply wireless nodes functionality, would fill a significant part of the technology gap limiting the wide diffusion of efficient and cost effective IoT applications. Such demanding targets can be reached through integration of heterogeneous technologies aiming to fully autonomous objects, especially in terms of self-powering, for which combination of energy harvesting (EH) and ultra-low power (ULP) technologies play a key role (Beeby and White 2010). The focus of this paper is condensed around the discussion of a novel design concept for high-performance wideband MEMS (MicroElectroMechanicalSystems) based vibration Energy Harvesters (EH-MEMS). As it will be extensively discussed in the following, power specifications of the proposed EH-MEMS concept comply with typical requirements of modern ULP WSN. Therefore, its exploitability in IoT oriented application can contribute to the realization of self-powered energy-aware integrated sensing nodes.

The paper is arranged as follows. Section 2 reports a brief review of the current state of the art in EH with a special focus on micro-scale devices (MEMS technology) and vibration-based converters. Section 3 introduces some mechanical fundamental notions of inertial generators. Section 4 develops more details of the FLC EH-MEMS design concept and working principles. Section 5 discusses modelling and simulation of the studied device performed within the ANSYS Workbench™ framework. Section 6 reports details around the technology platform employed for the fabrication of FLC EH-MEMS physical samples. Section 7 shows the results of experimental tests conducted on the manufactured device samples, with the twofold aim of proving the FLC expected performance and validating the modelling approach. Section 8 eventually collects some conclusive considerations, remarks and future perspectives of the whole work.

2 State of the art in MEMS-based vibration energy harvesting

Energy harvesting (EH), also known as energy scavenging (ES), literally means to extract energy from the surrounding environment and convert it into electric power. The ambient scattered energy can typically be attributed to four different sources (Vullers et al. 2010): (1) vibration/motion, both human and industrial (e.g., human pace, domestic/industrial appliances' vibrations); (2) thermal energy, both

human and industrial (e.g., skin temperature, engine heat) (Percy et al. 2014); (3) ambient light, both indoor and outdoor (e.g., artificial light and sun radiation) (IXYS Solar Cell Products 2015; Prabha et al. 2011); (4) electromagnetic and radio frequency—RF (e.g., GSM base stations) (Collado and Georgiadis 2013; Popovic et al. 2013).

Despite the current state of research features relevant achievements in all the just listed categories, the content of this section will be mainly devoted to vibration EH and to the miniaturization of EH devices, in order to tailor the state of the art survey to the MEMS device concept discussed in the following pages. Vibration based energy harvesting, i.e., the conversion of mechanical energy scattered in the environment into electrical energy, represents a research stream of particular interest in modern wireless devices and networks. Starting from mid-Nineties, the interest of research commenced to focus on the realization of energy autonomous strategies for electronic devices. The solution reported in (Kymissis et al. 1998) exploits a piezoelectric energy converter housed in athletic shoes. It is one of the first relevant examples of environmental EH devoted to powering electronic modules. Since then, research on vibration based EH devices took significant steps forwards, fed by the continuous decreasing trend in Integrated Circuits (ICs) power consumption, making the scenario of self-powered (wireless) devices (Roundy et al. 2004) and traditional batteries replacement possible. Given these considerations, next challenges for vibration EHs are, namely, miniaturization and integration with active electronics, opening up the floor to massive exploitation of MEMS and Microsystem technologies. There are three methods to convert vibrations of EH-MEMS into electric power: piezoelectric, electromagnetic and electrostatic (Kamierski and Beeby 2010). In the first case, the piezoelectric effect is exploited to extract electricity from the mechanical vibration of a suspended proof mass (Erturk and Inman 2011). In electromagnetic scavengers, instead, the oscillation of a permanent magnet induces an electric current in a coil (Tao et al. 2012). Finally, the electrostatic transduction is based on charge displacement in two capacitor electrodes in relative movement (Liu et al. 2012). Obviously, shrinking down dimensions from macro to micro domain brings a dowry of numerous pros and cons. First, scaling down devices footprint means reducing the harvested power. At first sight, this looks like a disadvantage. Nonetheless, if, on one side, supply of low power and ULP electronics is less and less demanding (as mentioned above), on the other hand, development of microfabrication technologies enables to enhance energy conversion efficiency of MEMS based vibration EHs. To this end, piezoelectric conversion in the micro domain exhibits power densities that are even larger than traditional macro devices, as reported in (Zhu 2011). On the contrary, electromagnetic (Cugat et al. 2003) and electrostatic micro devices are in general

less performing, despite also less mature, if compared to piezoelectric solutions (Zhu 2011), and thereby still admit considerable margins of improvement. Another issue arising from miniaturization of EHs is the scaling of operating frequency. As is well-known, resonant frequency of a vibrating device increases when mass and geometry are shrunk (Kamierski and Beeby 2010). On the other hand, most part of ambient vibration energy is available below a few kHz (e.g., busy street, car engine, industrial/domestic appliance, etc.) (Roundy et al. 2004). State of the art solutions to circumvent this problem are available. They are based on up conversion of ambient vibration frequency until reaching the converter resonance. For instance, this is achieved by exploiting complementary magnets (Galchev et al. 2012), or by designing the mechanical structure so that snap (Fu et al. 2012; Zorlu et al. 2011) and buckling induced pulses (Chamanian et al. 2012) are imposed to the micro converter. Additional solutions directed to widen EHs' vibration spectrum of sensitivity are also discussed in literature. By making the elastic behaviour of a vibrating mass non-linear, the device frequency response exhibits a chaotic behaviour (duffing mode resonance) (Halvorsen 2012). This extends the frequency range of operability and, in turn, the level of extracted power (Hajati et al. 2011; Goldschmidtboeing et al. 2009). Moreover, tuning of the EH resonant frequency is also studied to maximize extraction in the widest possible range of operability (Todorov et al. 2011). Concerning technology, the scientific literature is populated by findings in the field of material science and thin-film deposition techniques, resulting in relevant improvements in power conversion of vibration EHs. Starting from piezoelectric materials, the optimization of deposition conditions (e.g., temperature, grain growth) (Akiyama et al. 2009; Zukauskaite et al. 2012), conditioning of the substrate surface (Schneider et al. 2012) and in patterning of layers (i.e., interdigitated) (Chidambaram et al. 2012) or a tailored top electrode design (Mayrhofer et al. 2015; Sanchez-Rojas et al. 2010) reflects in large enhancements of piezoelectric response. Concerning electrostatic (i.e., capacitive) EHs, the conversion capabilities are importantly boosted by deposition of densely charged electrets, i.e., permanently charged/polarized dielectric layers (Hagiwara et al. 2012; Suzuki et al. 2011). Finally, miniaturized electromagnetic scavengers previously considered not successful because of scaling issues (Cugat et al. 2003), recently started to benefit from the development of efficient techniques for patterning (Miki et al. 2012) and bonding (Tao et al. 2012) of thin layers with improved magnetic properties. This increases the magnet to coil coupling, and, in turn, the EHs performance. Given the rather wide scenario depicted above, the focus of this work is confined around operability extension of EH-MEMS devices. This is achieved by means of the pronounced converter sensitivity distributed on a wide range of excitation frequencies. The

target can be reached by referring to a couple of different fashions. On one side, redundant employment of MEMS resonators with varied suspended mass and/or elastic constant extends frequency operation of the whole array (Chandrahalim and Bhave 2008). On the other hand, another viable solution consists in designing the MEMS mechanical structure in such a way to exhibit a large number of resonant modes in a certain frequency range (i.e., multi-modal resonant structure) (Brennen et al. 1990; Casset et al. 2009). In most cases the number of mechanical Degrees Of Freedom (DOFs) is increased by replicating the EH base element with slightly modified geometrical features according to array-like arrangements, as reported in (Kim et al. 2011; Shahruz 2006; Ferrari et al. 2008; Xue et al. 2008; Qi et al. 2010). The main drawback of this strategy is the increase of area occupation due to the presence of multiple devices. On the contrary, the EH-MEMS concept discussed in the following pages exploits the latter design-level solution (i.e., increase of mechanical DOFs (Ou et al. 2010)) to achieve multi-modality, without replicating the MEMS device, but rather acting on the geometry of a unique mechanical resonator. This ensures both high-performance in terms of power conversion in a wide frequency range of vibrations, as well as compactness of the whole EH converter.

3 Fundamentals of inertial generators

As extensively discussed in literature, inertial generators can be suitably modelled as second-order mass-spring systems. A general schematic representation is depicted in Fig. 1, where k denotes the spring stiffness, m the seismic mass, and c the cumulative energy losses of the system, e.g., due to viscous damping and electrical energy extraction.

Typically, the excitation ($y(t)$ in Fig. 1) is applied to a frame that embodies the generator, resulting in the $z(t)$ displacement of the latter one. The differential equation of motion of the system can be expressed as (Beeby and White 2010):

$$m\ddot{z}(t) + c\dot{z}(t) + kz(t) = -m\ddot{y}(t) \tag{1}$$

The energy is extracted by the converter when it is in relative movement with respect to the external frame, thus leading to the following formulation of the vertical displacement:

$$z(t) = \frac{\omega^2}{\sqrt{\left(\frac{k}{m} - \omega^2\right)^2 + \left(\frac{c\omega}{m}\right)^2}} Y \sin(\omega t - \varphi) \tag{2}$$

where ω and Y are the frequency and the amplitude of the stimulus applied to the frame, respectively, while the phase angle ϕ is:
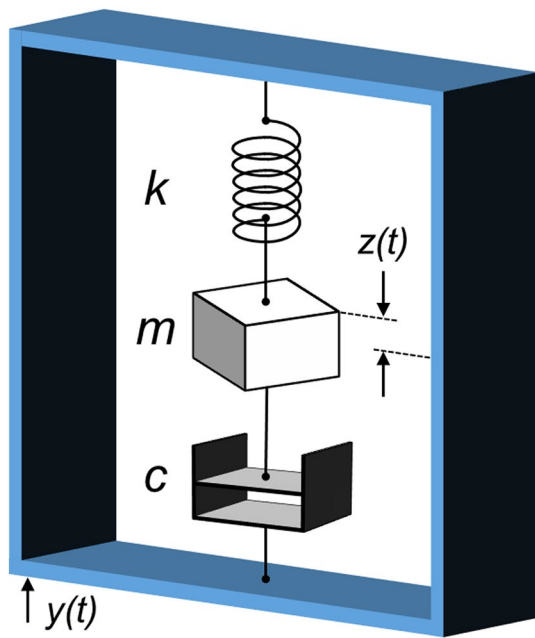
Fig. 1 Schematic of a generic second-order mass-spring system often used to model inertial generators. In figure, k, m and c represent the spring elastic constant, proof mass and damping effects, respectively. Moreover, $y(t)$ is the excitation the inertial frame is subjected to, while $z(t)$ is the net displacement of the inertial generator
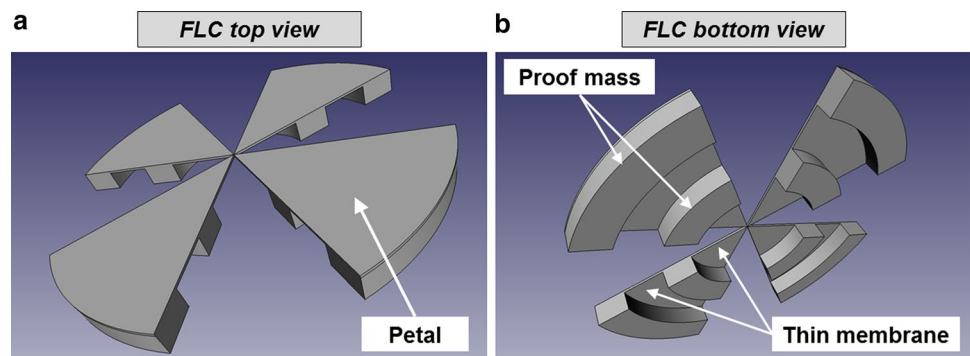
$$\varphi = \tan^{-1} \left(\frac{c\omega}{k - \omega^2 m} \right) \tag{3}$$

The power extracted by the converter (P_e) is maximum when it oscillates at the natural resonant frequency of the system (ω_r), and when the mechanically induced damping factor ζ_m equals the electrically induced damping factor ζ_e, due to extraction of power from the converter (Beeby and White 2010):

$$P_e = \frac{m \zeta_e A^2}{4 \omega_r (\zeta_m + \zeta_e)^2} \tag{4}$$

where A is the acceleration expressed as $A = \omega_r^2 Y$.

4 The four-leaf clover (FLC) EH-MEMS design concept

The EH-MEMS novel design concept discussed in this work is named four-leaf clover (FLC) after the resemblance it bears to a clover with four leaves, as shown in Fig. 2a. Each petal realizes a double-cascaded mass-spring mechanical resonator, as shown in Fig. 2b. Deformable parts (i.e., springs) are constituted by thin silicon membranes, while proof masses are implemented in thick (non-deformable) silicon.

The particular shape of the FLC EH-MEMS device is chosen to increase the number of mechanical DOFs, thus allowing multiple resonant mode configurations for the resonator, and extending, in turn, operability of the EH in terms of vibration frequency range (i.e., wideband converter). The schematic view in Fig. 2 reports the sole intrinsic FLC mechanical resonator. In order to be usable, real devices are completed with four tapered thin membranes joined to the centre of the resonator, that anchor the whole structure to the surrounding thick Silicon frame, as shown in the schematic in Fig. 3.

Since the FLC EH concept is conceived to exploit piezoelectric effect as mechanical into electric power conversion mechanism, presence of multiple resonant modes can in principle ensure distribution of mechanical strain within deformed parts of the structure, for a wider range of vibrations. This increases the device power conversion performance, as discussed more in detail in the following pages.

5 FLC EH-MEMS Simulation and Behavioural Analysis

In this section, the mechanical and multiphysics (i.e., mechanical and electrical) behaviour of the FLC EH-MEMS device concept is investigated by means of Finite Element Method (FEM) simulation performed in ANSYS Workbench™. The good level of accuracy achievable by
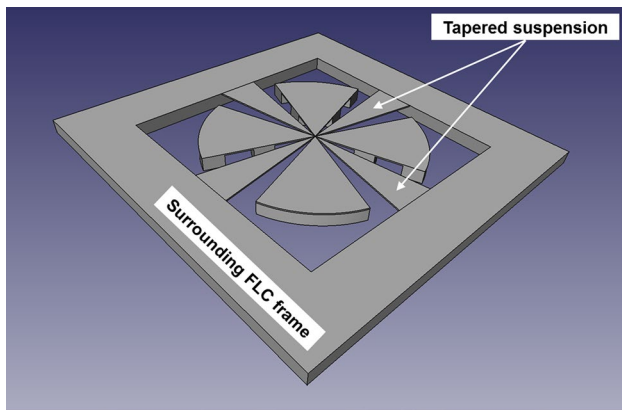
Fig. 2 a Schematic *top view* of the FLC EH-MEMS mechanical multi-resonator concept; **b** *bottom view* of the FLC showing thin deformable membranes (i.e., springs) and proof masses

Fig. 3 Schematic of the complete FLC EH-MEMS that includes the intrinsic multi-modal mechanical resonator, four tapered thin membrane suspensions and the surrounding thick Silicon frame

means of the adopted simulation methodology has been already validated by the authors with reference to the first FLC only mechanical (i.e., without piezoelectric thin-film layer) resonator physical test structures, as reported in (Iannacci et al. 2014). As case study, a starting not fully optimized FLC design (i.e., first guess) is considered for simulations, according to the geometrical features of petals and suspensions shown schematically in Fig. 4, and listed quantitatively in Table 1.

The first performed analysis is a modal (eigenvalues) simulation, aimed to identify FLC's resonant frequencies and the associated deformed shapes. In order to reduce computational load and simulation time, the Silicon thick surrounding frame (see Fig. 3) is suppressed in the Workbench 3D model, as it is meant to be the anchor of the FLC intrinsic resonator and it does not contribute to its dynamic response. Suitable Boundary Conditions (BCs) are imposed

Fig. 4 Schematic of a quarter of FLC (i.e., petal and suspension), where all the geometrical DOFs are highlighted and listed. Detailed explanation of each symbol and numerical values of DOFs are listed in Table 1
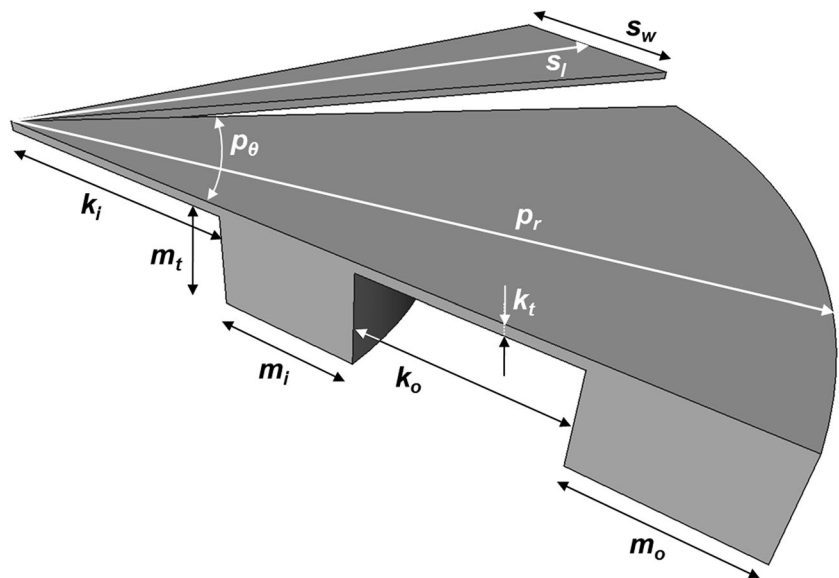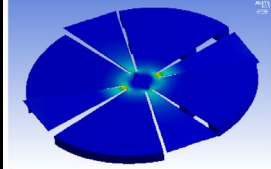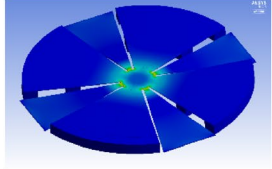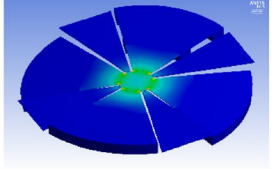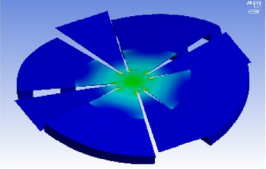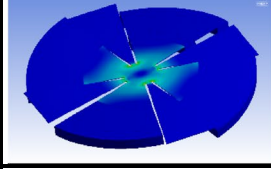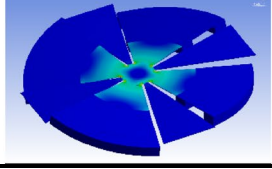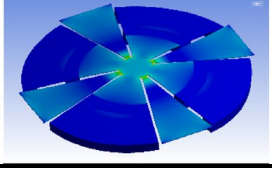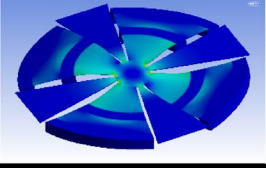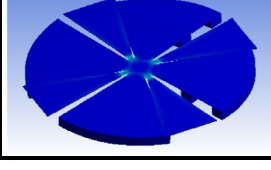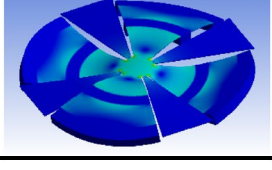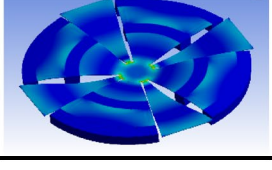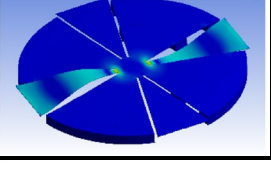

Table 1 Qualitative description and quantitative values of the geometrical DOFs of the intrinsic FLC (i.e., petal and suspension) used in the case study discussed in this section

DOF (see Fig. 4)	Description	Value
k_i	Length of the inner petal's deformable spring	2000 μm
k_o	Length of the outer petal's deformable spring	1000 μm
m_i	Length of the inner petal's proof mass	500 μm
m_o	Length of the outer petal's proof mass	500 μm
k_t	Thickness of the FLC deformable membrane	20 μm
m_t	Thickness of the FLC proof masses	350 μm
p_r	Radius of the petal	4000 μm
p_θ	Angular aperture of the petal	60°
s_l	Length of the tapered triangular suspension	4200 μm
s_w	Width of the suspension at joint with surrounding frame	2000 μm

Table 2 FLC 3D deformed shapes and frequencies corresponding to the resonant modes predicted by eigenvalues simulation in workbench

Mode 1 – 259 Hz – YES	Mode 2 – 302 Hz – YES	Mode 3 – 366 Hz – YES	Mode 4 – 975 Hz – YES
Mode 5 – 996 Hz – YES	Mode 6 – 1.32 kHz – YES	Mode 7 – 1.47 kHz – YES	Mode 8 – 4 kHz – YES
Mode 9 – 4.37 kHz – NO	Mode 10 – 4.62 kHz – YES	Mode 11 – 10.2 kHz – YES	Mode 12 – 11.6 kHz – NO

Colour gradient corresponds to the concentration of equivalent elastic strain on the FLC top surface (i.e., *blue* no strain, *red* high strain). The "YES" or "NO" indication highlights the estimated effectiveness of each resonant mode for piezoelectric energy conversion

to the FLC by applying mechanical constraints (i.e., zero displacement in all directions) to the outer vertical faces of the four triangular suspensions (i.e., along s_w in Fig. 4). The results of the modal FEM analysis are reported in Table 2.

In order to enable efficient conversion of vibrations into electrical energy, mechanical strain should be as intense as possible in the device regions where the piezoelectric thin-film is deposited. For this reason, equivalent elastic strain on the FLC surface is displayed in Table 2 with colour gradient for all the observed modal shapes (where blue means no strain, while red indicates high strain). To help understand the reported information, the "YES" or "NO" labels indicate per each mode if it is supposed to be effective or not, respectively, for piezoelectric energy conversion. As visible, most of resonant modes exhibit significant distribution of strain in the inner petals' membranes (k_i in Fig. 4), suggesting good power conversion capabilities, already commencing from vibration frequencies as low as 260 Hz. Starting from around 4 kHz, also the outer petals' membranes (k_o in Fig. 4) show relevant strain concentration, suggesting further increase of converted power. In particular, modes 8, 10 and 11 clearly highlight the presence of a circular belt on petals where there is no strain concentration (blue colour), corresponding to where inner proof masses (m_i in Fig. 4) are located. This happens because where the Silicon is thick it tends not to deform, but to rigidly move in the out-of-plane direction. Among all the studied resonant frequencies, just two modes are not expected to give significant contribution to piezoelectric energy conversion. Indeed, mode 9 at 4.37 kHz is characterized by rotation of

petals around vertical axis, confining strain just close to the joint with suspensions, while mode 12 at 11.6 kHz exhibits vertical deformation of triangular suspensions rather than of petals. Resonances taking place above 10-11 kHz are purposely not studied, as vibrations scattered in the surrounding environment typically do not reach higher frequencies, and in any case the energy available above this range is often quite low. According to the results of the Workbench modal analysis, the FLC EH-MEMS device concept is expected to exhibit good power conversion capabilities in correspondence to multiple resonant modes scattered in a range of vibrations from 260 Hz up to around 10 kHz (i.e., wideband operation). Such characteristic is now going to be further investigated by means of multiphysics harmonic analysis in ANSYS Workbench.

The same 3D Workbench model used for modal analysis is employed also for harmonic simulations, as it already counts in the mechanical properties of a 1 μm thick AlN layer defined above the Silicon FLC resonator. Nonetheless, differently from eigenvalues analysis where multiphysics behaviour is not studied, piezoelectric transduction across mechanical and electrical physical domains must be modelled and implemented. To do so, we employ hybrid approach allowed by the simulation framework that integrates portions of command lines written in ANSYS Parametric Design Language (APDL) (ANSYS Parametric Design Language (APDL) 2015) within the project tree defined in Workbench. This enables full exploitation of ANSYS Classic descriptive potentialities within the Workbench Graphic User Interface (GUI) environment. At first,
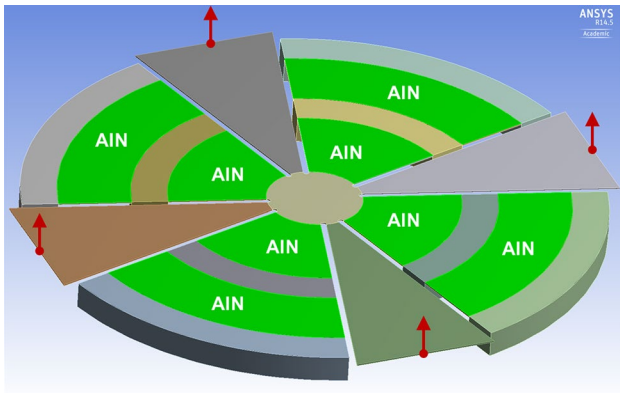
Fig. 5 Schematic of the FLC 3D model as defined in Workbench. A subset of eight electrodes is selected in the AlN physical layer, corresponding to the flexible parts of each petal (i.e., k_i and k_o in Fig. 4). The four *vertical arrows* at the suspensions edges indicate the mechanical stimulus (i.e., displacement) imposed to the FLC structure in the harmonic simulation

we generated a part in the AlN physical layer, grouping a subset of areas as indicated in the FLC Workbench 3D model shown in Fig. 5.

As visible, only the AlN surface above thin Silicon of each petal (i.e., k_i and k_o in Fig. 4) is considered for modelling of piezoelectric transduction. As emerged during modal analysis (see Table 2), proof masses give no contribution to the accumulation of surface elastic strain, and, in turn, to the generation of electric charges. Subsequently, we defined three groups of APDL commands to model the multiphysics piezoelectric transduction, as follows:

- Group 1. In the geometry section of the project tree, after determining the selection of areas reported in Fig. 5, we associated to it APDL commands to define the AlN mechanical and electrical/piezoelectric properties (listed in Table 3). Moreover, we selected the SOLID226 element (Kutiš et al. 2012) to mesh the AlN layer, since it manages to model piezoelectric effect, coupling the mechanical and electrical physical domains;

- Group 2. In the harmonic response section of the project tree, we included APDL commands to define electrical BCs for the selection of electrodes in Fig. 5. In particular, we forced 0 V on the bottom face of the AlN (ground), while we selected and separately grouped all the nodes on the top faces of the eight AlN electrodes, as we want to read the generated voltage in response to mechanical deformation of the piezoelectric layer. This approach allows to treat the electrical behaviour of each electrode independently from all the others and, therefore, to monitor the power generated by each AlN surface in response to the deformation of the whole mechanical structure. Furthermore, we are interested to simulate the FLC power conversion capabilities in real operation conditions. To do so, rather than monitoring the generated output voltage on the AlN top and bottom electrodes in open circuit configuration, we defined a purely resistive load connecting them. The lumped resistor is defined in APDL by inserting the CIRCU94 element (Zhu et al. 2009), and the load is set to 100 kΩ, it being a reasonable value, as reported in literature (Janphuang et al. 2014). Further experimental investigations on the optimal load impedance matching, in order to improve the FLC power conversion performance, have recently been performed by the authors, as reported in (Iannacci and Sordo 2016);

- Group 3. Eventually, in the solution section of the project tree, we grouped a few APDL command lines in order to read the voltage drop on the AlN top and bottom faces at each frequency iteration, calculate the generated power, and append such information in an output data file.

In order to complete the information concerning harmonic analysis, mechanical and electrical properties of

Table 3 Mechanical and electrical properties of the silicon (considered isotropic in FEM simulations) and AlN layers used in the harmonic simulation of the FLC EH-MEMS

Material property		Value
Silicon	Young's modulus	130 GPa (Beigelbeck et al. 2014)
	Poisson's ratio	0.28
	Density	2440 kg/m³
Aluminium nitride (AlN)	Young's modulus	250 GPa (Schneider et al. 2014)
	Poisson's ratio	0.24
	Density	3260 kg/m³
	Relative dielectric constant	10.5
	d_{31} piezoelectric coefficient (AlN thickness ranging from 500 nm to 1 μm)	$-1 \div -1.3$ pm/V (Ababneh et al. 2010)

Fig. 6 Outcome of the Workbench harmonic simulation (displayed up to 5 kHz) concerning mechanical into electric power conversion operated by the inner and outer AlN electrodes (see Fig. 5) belonging to one of the four petals
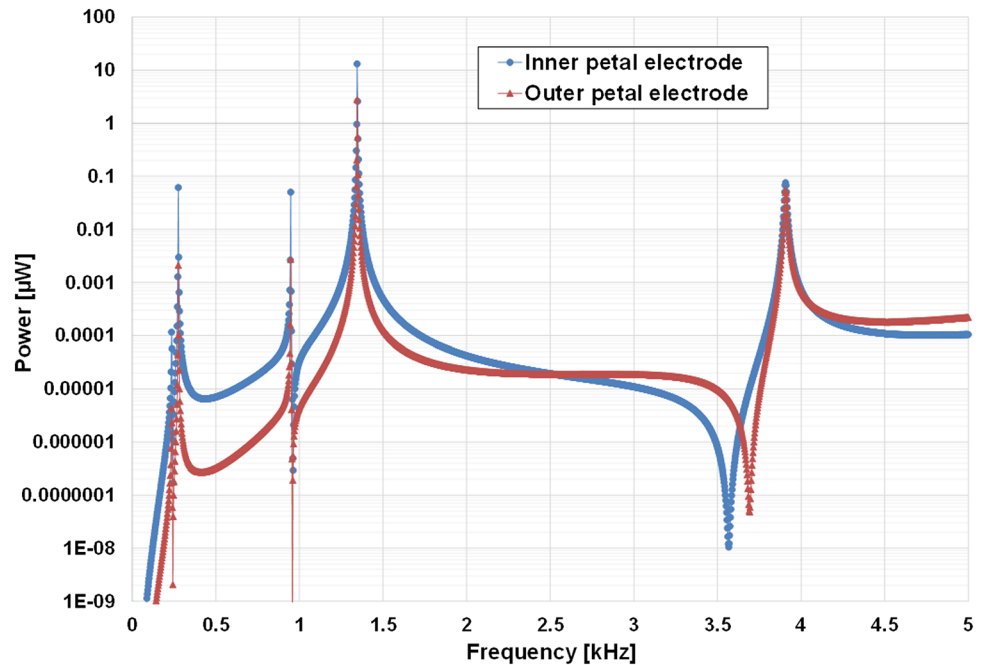
the materials constituting the FLC 3D model are listed in Table 3.

It must be stressed that, despite the Silicon employed for the realisation of the EH physical samples exhibits anisotropic mechanical properties, in the FEM simulations the material was approximated as isotropic. This simplification is built upon the assumption that the FLC structure is characterised by rather large dimensions, if compared to typical MEMS resonators. Moreover, the EH is always simulated considering viscous air damping at ambient conditions (i.e., low quality factor). Therefore, given such a context, the mechanical effects due to the intrinsic properties of the material can be neglected. In any case, the appropriateness of the just mentioned assumptions is proven by the rather accurate prediction of the FLC dynamics realised by the FEM 3D model, when compared against experimental data, as it will be shown later in Sect. 7. The harmonic simulation of the FLC EH-MEMS that is going to be discussed is performed in the frequency range up to 10 kHz. The mechanical stimulus imposed to the structure is a vertical displacement (along the Z-axis) of 1 μm, applied to the vertical faces of the four tapered suspensions, as shown in Fig. 5. In order to reproduce a consistent condition as if the Silicon surrounding frame was included, in-plane displacements (X- and Y-axis) of such faces are forced to zero. Finally, to stimulate FLC's resonant modes non-symmetric with respect to the vertical axis, a phase delay of 30° is set between adjacent vertical displacements imposed to the suspensions (i.e., 0°, 30°, 60°, 90°). The Workbench conversion outcome is reported in Fig. 6, where the power generated by the inner and outer AlN electrodes, both

belonging to one of the four petals (see Fig. 5), is plotted against frequency. Despite the simulation was performed up to 10 kHz, the converted power is plotted up to 5 kHz in order to help interpret the results.

The plot in Fig. 6 shows the presence of multiple resonant modes up to around 4.5 kHz. In the model below 1 kHz the inner AlN electrode exhibits higher values of converted power (Root Mean Square—RMS) compared to the outer one, in any case below 100 nW. This consideration still holds validity at 1.35 kHz, where the inner and outer electrode generate 13.2 and 2.8 μW, respectively. Finally, in the last resonance displayed in Fig. 6 (3.9 kHz) the conversion capability of both electrodes drops to around 75 nW. In light of the just reported results, a few additional considerations should be kept in mind. First, the mechanical BCs imposed to the FLC in the harmonic simulation are rather conservative (1 μm vertical displacement). In real application scenarios larger displacements and accelerations can be expected, and, in turn, higher levels of power converted by the discussed EH-MEMS. Then, the curves reported in Fig. 6 refer to just one of the four FLC's petals (i.e., two out of eight AlN electrodes). This means that the performance of the entire device in terms of mechanical energy into electric power conversion is around four times better than what reported above. In any case, the approach of managing separately each AlN electrode is certainly more efficient from the conversion efficiency point of view. Presence of multiple resonant modes, indeed, leads to anti-symmetric deformed configurations of the mechanical structure (see Table 2) that cause cancellation effects of the charge generated by the piezoelectric material, thus

Fig. 7 Shear elastic strain (XY-plane) on the surface of a single petal inner AlN electrode (see Fig. 5) compared against the one calculated over all eight piezoelectric electrodes (four petals)
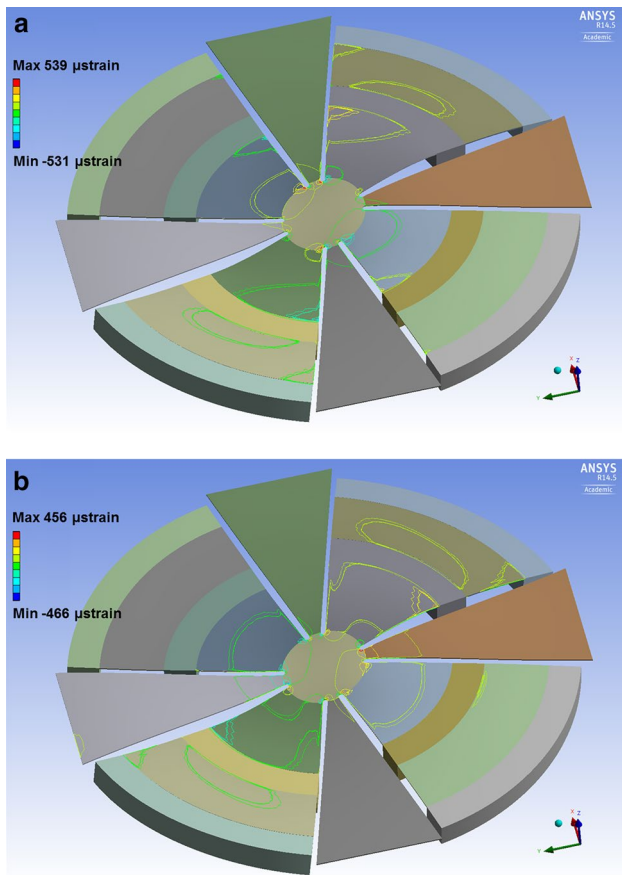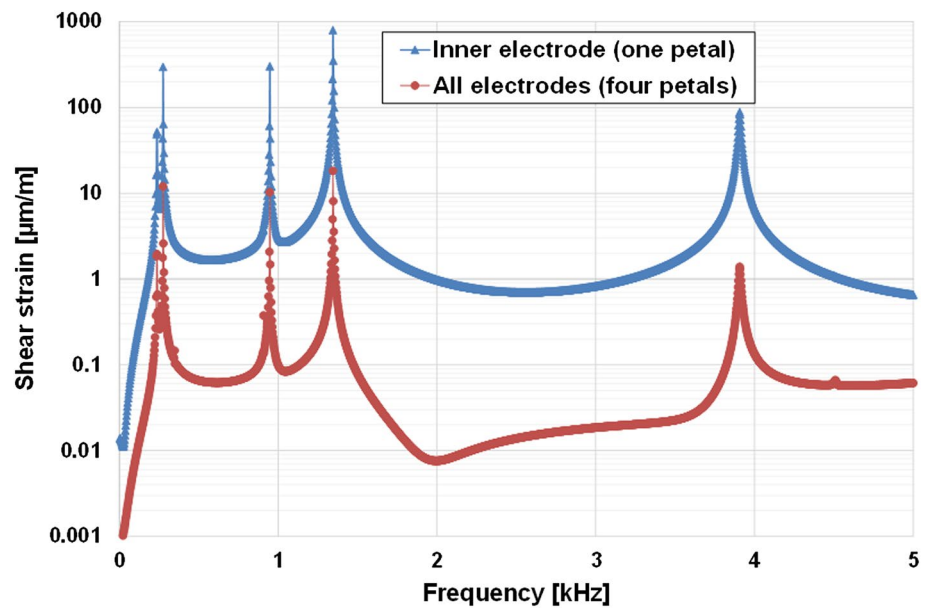

Fig. 8 In-plane normal elastic strain (isosurface) on the FLC surface captured during the deformation of two opposed petals occurring at 3.9 kHz, **a** along the X-axis direction; **b** along the Y-axis direction

reducing power conversion efficiency. Therefore, patterning and separation of electrodes on the mechanical resonator surface have to be carefully defined in order to optimize the extracted power, as discussed in (Lee et al. 2007; Chidambaram et al. 2013). This issue emerges clearly in the plot in Fig. 7, where the shear elastic strain calculated on one AlN electrode (inner single petal) is compared against the one resulting from all eight electrodes (four petals).

It is evident that the amount of shear elastic strain (effective for piezoelectric conversion) over a single AlN electrode is larger than that of all eight electrodes, it being e.g., 800 µstrain (i.e., µm/m) in the first case and 18 µstrain in the latter one, for the resonant mode occurring at 1.35 kHz. Eventually, Fig. 8 shows the in-plane normal elastic strain (isosurface) on the FLC surface, in correspondence to the reverse deformation of two opposed petals at 3.9 kHz, split along the X-axis (Fig. 8a) and Y-axis (Fig. 8b).

It is visible that the FLC top surface corresponding to the proof masses does not contribute significantly to the accumulation of strain because of their elevated stiffness. Therefore, the presence of AlN on those areas would imply negligible benefit for the power conversion capability of the EH-MEMS. This explains why electrodes were considered as shown in Fig. 5. On the other hand, isosurface areas indicate concentration of in-plane normal strain, both concerning the X-axis (Fig. 8a) and Y-axis (Fig. 8b) directions, in correspondence to the flexible membranes where the piezoelectric material is deposited. Normal strain values range between around ±500 µstrain concerning both cases reported above.

6 Fabrication of FLC physical samples

Physical samples of FLC EH-MEMS are fabricated at the
Institute of Sensor and Actuator Systems (ISAS), Vienna
University of Technology (VUT). The process is a com-
bination of surface and bulk micromachining steps per-
formed on 4 inch silicon on insulator (SOI) wafers, and the
sequence is schematically reported in the 3D sketches in
Fig. 9. In order to ease the understanding of the process,
the simplified case of a cantilever with a proof mass at the
free end is considered, and some manufacturing phases not
linked to lithography steps are omitted.

As shown in Fig. 9a, processing starts with SOI wafers
(20 μm of device layer; 1 μm of buried oxide; 350 μm
of handle layer), on top of which an insulating stress

compensated bi-layer of Silicon Oxide and Silicon Nitride
is deposited (not shown in figure). Thereafter, bottom con-
ductive electrode (500 nm thick gold) is evaporated and
patterned (see Fig. 9b). Aluminium Nitride (AlN) piezo-
electric layer (thickness around 500 nm and 1 μm) is then
sputtered and patterned (see Fig. 9c), and top conductive
electrode (500 nm thick gold) is subsequently evaporated
(see Fig. 9d). After the surface micromachining process-
ing, definition of the mechanical resonant structure is per-
formed by deep reactive ion etching (DRIE) of silicon sub-
strate (i.e., bulk micromachining). In particular, the SOI
handle layer is selectively etched from the back side in
order to define deformable membranes (i.e., thin Silicon)
and proof masses (i.e., thick Silicon), as shown in Fig. 9e.
Eventually, front side selective etching of the SOI device

layer (DRIE) and of the buried oxide (wet etching) releases the final mechanical structures (see Fig. 9f). To conclude this section, the photograph of two different FLC physical samples mounted (and wire-bonded) on Printed Circuit Boards (PCBs) is reported in Fig. 10. In particular, both design concepts with straight beam (Fig. 10a) and tapered (Fig. 10b) suspensions are shown.

7 Experimental characterization

In this section, experimental activities conducted on the first FLC EH-MEMS fabricated samples are reported and discussed. The design of reference for all the data reported below is different from the one discussed so far and detailed in Table 1. Apart from modified ratios of proof masses and membranes along petals, the FLC here analysed presents straight beam suspensions rather than tapered ones. All the details of the samples used for experimental testing are listed in Table 4.

The mechanical behaviour of the FLC specimens is investigated at first with a Laser Doppler Vibrometer (LDV) setup (Polytec MSA 400). The Device Under Test (DUT) is stimulated with a piezoelectric shaking actuator housed underneath it, and all the samples are measured in air. The LDV detects real-time vertical displacement, velocity and acceleration of a matrix of points placed on the surface of one of the four FLC's petals, and averages the measured data. Moreover, the FLC surrounding frame (see Fig. 3) is also measured by the LDV, and its contribution is subtracted from the petal's dynamic. In this way, it is possible to reconstruct the absolute displacement of the FLC EH-MEMS, ruling out the presence of the piezoelectric actuator. The latter one is controlled with a white noise

Table 4 Qualitative description and quantitative values of the geometrical DOFs of the intrinsic FLC (petal and suspension) physical samples experimentally tested and discussed in this section

DOF	Description	Value
k_i	Length of the inner petal's deformable spring	2100 μm
k_o	Length of the outer petal's deformable spring	400 μm
m_i	Length of the inner petal's proof mass	250 μm
m_o	Length of the outer petal's proof mass	1250 μm
k_t	Thickness of the FLC deformable membrane	20 μm
m_t	Thickness of the FLC proof masses	350 μm
p_r	Radius of the petal	4 mm
p_θ	Angular aperture of the petal	60°
s_l	Length of the straight beam suspension	4.1 mm
s_w	Width of the straight beam suspension	120 μm

voltage signal of 1 V amplitude and 500 mV offset, in order to have only positive voltage. The reason why we chose this type of stimulus is that it is closer to the typical vibration energy sources available in real application environments, if compared, for instance, to a CHIRP waveform. On the other hand, the FLC 3D model is simulated in Workbench (harmonic simulation) by imposing an acceleration to the whole structure with 5 m/s² components along the XYZ axes, corresponding to a modulus of less than 1 g. The plot in Fig. 11 compares the measured vertical displacement averaged by the LDV with the same magnitude calculated by Workbench on the petal's surface. The two traces are plotted on different vertical axes because the stimuli in the experiment and simulation are not comparable (white noise voltage vs. acceleration), and, therefore, the superimposition of the two traces holds qualitative value. Differently, the target of Fig. 11 is to provide quantitative indications

Fig. 11 Measured vs. simulated averaged vertical displacement detected on the surface of one FLC's petal. The amplitude of displacement can be compared just qualitatively because of different stimuli imposed in the experiment and simulation. On the other hand, good correspondence of the measured and simulated resonant frequencies is visible, mainly below 5 kHz
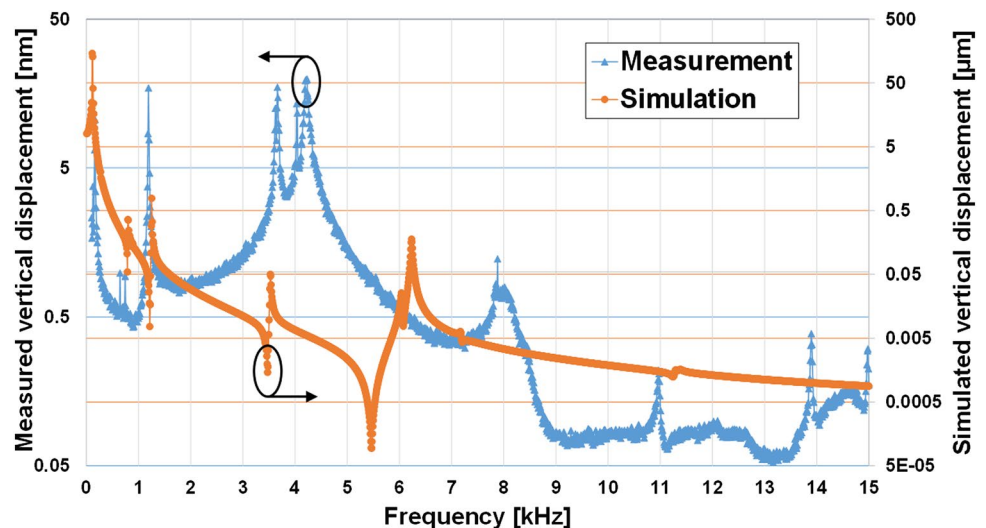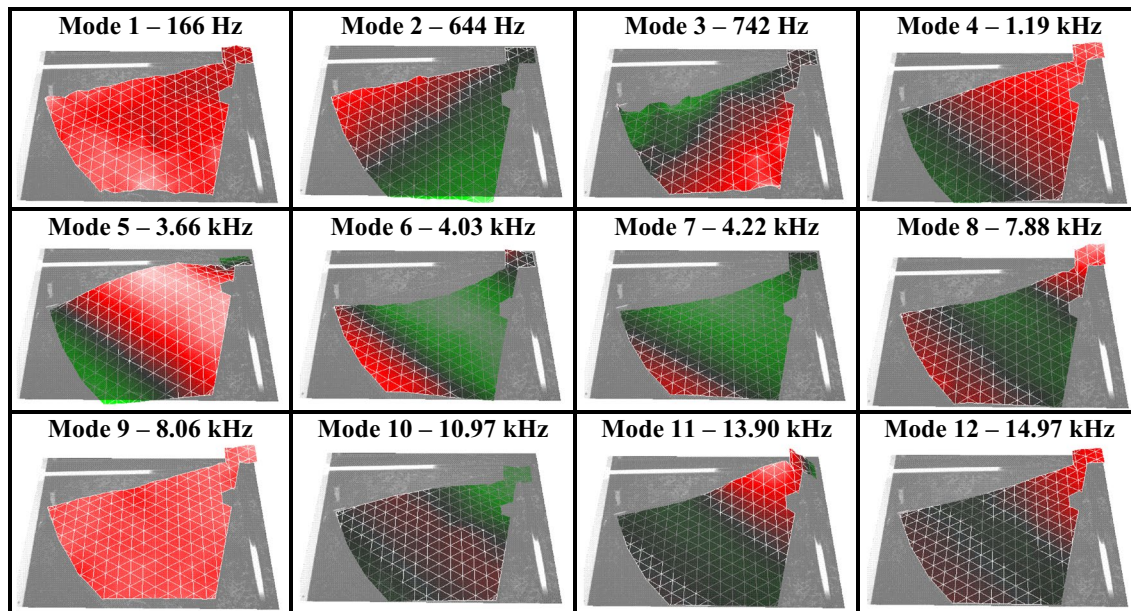
Table 5 Snapshots taken from the animations generated by the FLC software per each measured resonant mode

Mode 1 – 166 Hz	Mode 2 – 644 Hz	Mode 3 – 742 Hz	Mode 4 – 1.19 kHz
Mode 5 – 3.66 kHz	Mode 6 – 4.03 kHz	Mode 7 – 4.22 kHz	Mode 8 – 7.88 kHz
Mode 9 – 8.06 kHz	Mode 10 – 10.97 kHz	Mode 11 – 13.90 kHz	Mode 12 – 14.97 kHz

The surface of one petal is displayed and superimposed to the microphotograph (in *greyscale*) of one quarter of FLC (i.e., petal plus straight beams). The *colour scale* refers to vertical velocity of each measured point. In particular, *red* and *green* indicate upward (positive Z-axis) and downward (negative Z-axis) velocities, respectively, in the range up to ± 1.4 mm/s

about the accuracy of the Workbench model in predicting the frequency of the FLC resonant modes.

The Workbench model predicts all the measured FLC EH-MEMS resonant modes below 4 kHz with an error as large as 5 % in the worst case (i.e., at around 3.6 kHz). On the contrary, the simulation versus experiment correspondence is not particularly satisfactory above 5 kHz. In particular, the double measured peak in the range 4–4.2 kHz is not displayed in the simulated trace, and not even predicted by the Workbench modal analysis conducted on the same model (not discussed here for the sake of brevity). Moreover, the measured peak at around 8 kHz is underestimated by the harmonic simulation that predicts it at 6.24 kHz (error of 22 %). The correspondence between the simulated and measured deformed shape for this mode (see Table 5) was cross-checked with the Workbench modal analysis, thus confirming the rather large error mentioned above. On the other hand, the measured resonant modes above 8 kHz are not visible in the simulation because not triggered by the applied stimulus, but were in any case verified with the modal analysis. In summary, the predictive capability of the Workbench model seems to be more accurate in the lower frequency range, i.e. where we expect most part of the FLC EH-MEMS conversion capability to be scattered. Therefore, the employed simulation approach results to be appropriate for the DUT. Table 5 summarizes all the resonant modes (visible also in Fig. 11) detected by the LDV up to 15 kHz, showing the measured vertical velocity distribution of the points scanned on petal surface.

Such data confirm experimentally the presence of multiple resonant modes enabled by the FLC design concept. According to the considerations previously developed in this article (see Table 2), most of the deformed shapes reported in Table 5 are expected to lead to effective piezoelectric power conversion performance.

Finally, we report on the preliminary experimental characterization of the multiphysics (mechanical and piezoelectric) behaviour of the FLC EH-MEMS physical samples, by means of a testing setup currently under development at FBK. The measurement chain employs the TV 50018 vibration test system by Tira GmbH to shake the DUT, and laser displacement sensors by Keyence Corporation to observe its deformation (Romani et al. 2013; Dini et al. 2015). The FLC sample was mounted and wire-bonded on a PCB, in order to detect the voltage generated by the AlN deformation, and display it on the oscilloscope screen. Figure 12 shows the photograph of an FLC sample mounted on the PCB, and placed on the shaker plunger stage. Electrical interconnections from AlN electrodes to the external world are visible.

The plot in Fig. 13 shows the FLC mechanical and electrical behaviour in response to a sinusoidal waveform feeding the vibration test system at different frequencies. The DUTs are always measured in air and in standard ambient conditions.

More in details, Fig. 13 shows the normalized vertical acceleration of the FLC (main plot, left vertical axis). Such magnitude is the ratio between the vertical acceleration of
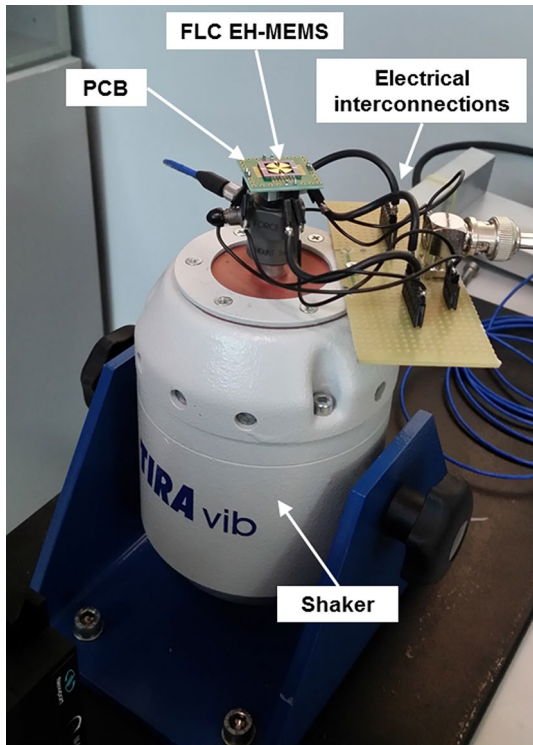
Fig. 12 Photograph of the FLC EH-MEMS physical sample mounted and wire bonded to a PCB, placed on the shaker stage, and wired in such a way to collect the electric signal generated by the AlN piezoelectric material and redistribute it to the external world

the FLC EH-MEMS, measured by the laser displacement sensor—the laser spot aims at a peripheral point of one FLC's petal—and the acceleration of the shaker support, detected via an accelerometer (by PCB Piezotronics Inc.) embedded in the vibration test system stage. This normalization was necessary because at the moment the measurement

system (still under development) does not feature any feedback control of the amplitude of the waveform powering the shaker on the basis of the acceleration imposed to the DUT. Therefore, when changing the frequency of the stimulus, the FLC was not subjected to constant acceleration. In any case, in the measurement shown in Fig. 13 the acceleration imposed by the shaker was ranging between 5.6 and 7.8 m/s^2. As expected, the FLC always amplifies the stage acceleration (ratio always larger than 1), and the value reaches its maximum in correspondence to the EH resonance at 193 Hz. On the other hand, the line referred to the vertical right axis in Fig. 13 shows the measured peak-to-peak voltage generated by the AlN electrodes deployed on the FLC petals. The maximum voltage output generated at resonance is of 87 mV. Since the resistive load of the oscilloscope is around to 1 MΩ (tested with a multimeter prior to the EH measurement), the FLC voltage would correspond to a generated RMS power of just 3.8 nW at 193 Hz. This outcome is not in line with what predicted by harmonic simulations (see Fig. 6). Nonetheless, a few considerations should be formulated in order to better interpret the just discussed results. In the first instance, the measurement setup shown in Fig. 12 allowed dynamic testing of the DUTs just in the low frequency range. Then, the sole observable resonant mode was the one occurring at around 190 Hz (see Fig. 13). As suggested by the LDV measurements previously shown in Table 5, the FLC deformed shape corresponding to the first resonant mode (in that case occurring at 166 Hz) is not expected to be well-suited for piezoelectric conversion. The four petals, indeed, tend to oscillate rather rigidly in the out-of-plane direction (i.e., along vertical axis). Such a configuration does not induce significant concentration of mechanical strain where the AlN electrodes are deployed (i.e., on the inner and outer petals' flexible membranes), but just on the suspending straight beams in correspondence to

Fig. 13 Main plot. Relative vertical acceleration of the FLC and peak-to-peak voltage generated by the AlN electrodes, in response to a sinusoidal waveform feeding the shaker. Subplot. FLC peak-to-peak voltage generated at resonance (190 Hz) for increasing values of acceleration imposed by the shaker stage to the DUT
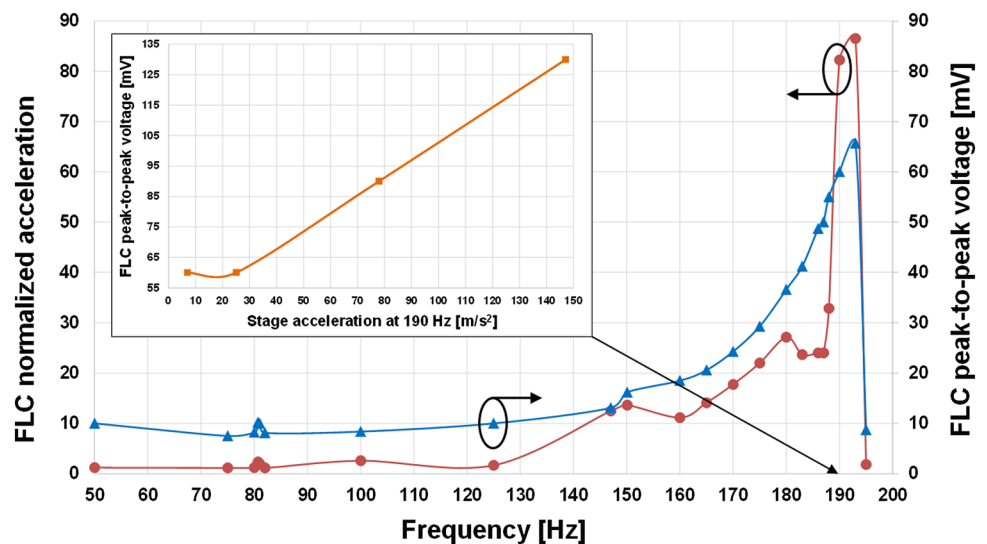
the petals-to-suspensions and suspensions-to-frame joints. Therefore, it must be kept in mind that the comparison between the measured plot in Fig. 13 and the simulated response in Fig. 7 holds just a qualitative value, also in light of the fact that it is referred to different FLC geometry configurations (see Tables 1, 4). On the other hand, the mechanical robustness of the FLC structural device resulted to be rather pronounced. The DUT underwent increasing accelerations up to 147 m/s^2 (i.e., around 15 g) at the fixed frequency of 190 Hz (see subplot in Fig. 13), without showing any mechanical failure. At the largest acceleration the FLC generated an output peak-to-peak of 130 mV, corresponding to RMS power of 8.45 nW. In order to support the just reported explanations, and also to perform further validation of the coupled field analysis method, the subplot in Fig. 13 was reproduced with harmonic simulations of the FLC performed in the same conditions of the physical devices (i.e., acceleration of different intensity at the fixed frequency of 190 Hz; resistance of 1 MΩ loading the AlN piezoelectric generator). The comparison between the measured and simulated voltage (peak-to-peak) generated by the FLC is reported in Fig. 14.

The plot exhibits a rather pronounced linearity of the peak-to-peak voltage generated by the FLC with respect to the intensity of the imposed acceleration, both for the measurement and the simulation. The two segments show a different slope (steeper in the case of the simulation), despite the order of magnitude of the voltage is correctly predicted by the simulation (from a few tens of mV to about 130–180 mV as the intensity of the acceleration ranges from about 10 to 150 m/s^2). Moreover, the deformed configuration of the FLC observable in the ANSYS Workbench simulation (not shown here for the sake of brevity) corresponds to the one measured and reported for the first mode in Table 5 and discussed above. This further evidence corroborates the considerations

previously developed, concerning the fact that the resonance measured with the setup in Fig. 12 is not particularly effective for piezoelectric conversion. To this regard, it must be stressed that, due to the still ongoing development of the measurement setup partially shown in Fig. 12, it was not possible to perform electric measurements of the FLC samples for higher frequencies up to 4–5 kHz. Thereby, no experimental evidences are available for what concerns the modes previously shown in Fig. 6. Nonetheless, the results shown in Fig. 14 prove that the modelling methodology employed for the FLC EH-MEMS is rather accurate also for what concerns coupled field analysis and piezoelectric conversion, and thereby that the performance previously reported in Fig. 7 are reasonable and achievable by the fabricated samples. In conclusion, the preliminary experimental tests reported in this section, despite do not fully implement comprehensive characterization of the fabricated samples, support complete proofing of the FLC EH-MEMS design concept. To this regard and in summary, the multi-modality of the mechanical resonator was experimentally demonstrated with LDV measurements, and simulations were validated on the basis of such results. Moreover, despite preliminarily, also the mechanical into electrical piezoelectric performance were experimentally tested and cross-checked with simulations, by means of ad-hoc measurement setup still under development. In the future, the just mentioned setup will be extended in such a way to fully characterize the AlN generator performance, and the results will be reported by the authors in an extension of this work.

8 Conclusions and further developments

In this work, we covered comprehensive discussion around a novel design concept of MEMS-based vibration Energy

Fig. 14 Comparison of the measured and simulated voltage (peak-to-peak) generated by the FLC when stimulated with an acceleration of increasing intensity imposed at 190 Hz, when the AlN generator is loaded with a resistor of 1 MΩ
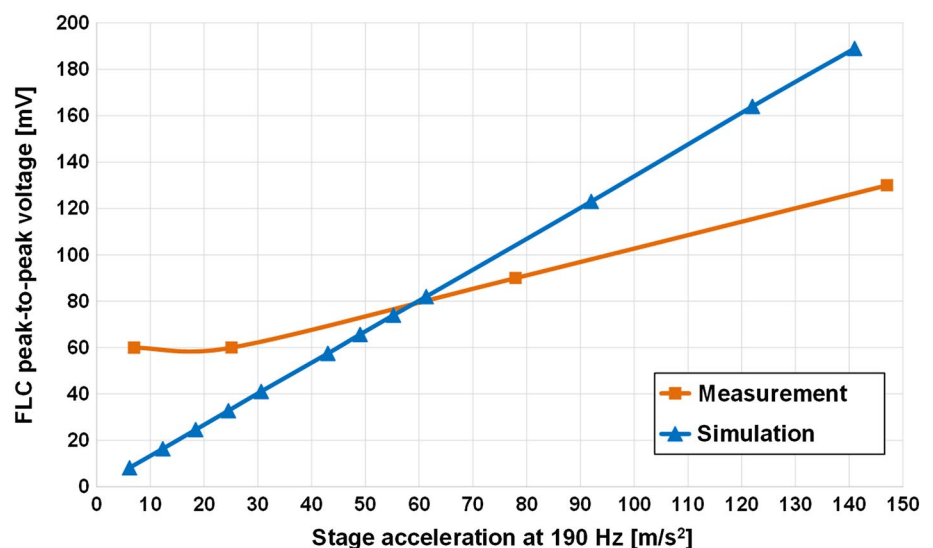
Harvester (EH), named Four-Leaf Clover (FLC EH-MEMS) after its circular shape featuring four petal-like mass-spring systems. The main goal of the FLC geometry is to enable multiple resonant modes in the frequency range of vibrations up to a few kHz, thus extending the device power conversion performance (i.e., wideband EH) and boosting the typical narrowband operability (around fundamental resonance) of cantilever-based EHs. The paper went through detailed discussion of several aspects linked to the development chain of the FLC EH-MEMS, starting from the elucidation of the design concept, and then focusing on Finite Element Method (FEM) multiphysics modelling and simulation, micro-fabrication of FLC physical samples, experimental characterization and validation of manufactured specimens.

Presence of multiple resonant modes of the FLC EH-MEMS was confirmed by FEM modal and harmonic simulation, as well as validated experimentally, in the frequency range up to 10–15 kHz. Nonetheless, not all such modes enable efficient mechanical into electric energy piezoelectric conversion, as some of them do not induce significant mechanical strain in the areas where Aluminium Nitride (AlN) is patterned onto the FLC surface. Such aspect was stressed in the contribution, as well as the occurrence of charge cancellation phenomena in correspondence to antisymmetric deformed shapes of the mechanical resonator. Thereafter, a fully optimized FLC design has to feature appropriate AlN electrodes pattern, as well as separate metal lines for redistribution of generated electric signals.

Concerning the mechanical behaviour of the FLC EH-MEMS, distribution of resonant modes as predicted by simulations, was proven to be in good agreement with experimental data collected by a laser doppler vibrometer (LDV) setup, especially in the frequency range up to a few kHz.

The reported experimental tests of the FLC power conversion performance just hold preliminary and qualitative value. Due to the limitations of the still under development measurement setup, just a very low-frequency (around 190 Hz) resonant mode was measured. According to LDV-based testing, such a resonance is not expected to be efficient for mechanical into electrical energy conversion. Given this premise, extracted power levels in the order of a few nW were experimentally demonstrated, and cross-checked with coupled field simulations. On the other hand, the FLC is expected to be able to convert power levels three orders of magnitudes better at resonance (μW instead of nW), as supported by comprehensive FEM coupled field modelling and analysis conducted in ANSYS Workbench.

Future developments of this work will include further experimental testing of the dynamic multiphysics behaviour of the fabricated EH-MEMS samples, in order to fully validate the energy conversion performance of the FLC concept in correspondence to all the resonant modes already tested with the LDV and reported in this paper.

References

Ababneh A, Schmid U, Hernando J, Sánchez-Rojas JL, Seidel H (2010) The influence of sputter deposition parameters on piezoelectric and mechanical properties of AlN thin films. Mater Sci Eng B 172:253–258

Akiyama M, Kano K, Teshigahara A (2009) Influence of growth temperature and scandium concentration on piezoelectric response of scandium aluminum nitride alloy thin films. Appl Phys Lett 95:1–3

ANSYS Parametric Design Language (APDL). http://www.mece.ualberta.ca/tutorials/ansys/AT/APDL/APDL.html. Accessed 15 May 2015

Beeby S, White N (eds) (2010) Energy harvesting for autonomous systems. Artech House, London

Beigelbeck R, Schneider M, Schalko J, Bittner A, Schmid U (2014) A two-step load-deflection procedure applicable to extract the Young's modulus and the residual tensile stress of circularly shaped thin-film diaphragms. J Appl Phys 116:1–13

Brennen RA, Pisano AP, Tang WC (1990) Multiple mode micromechanical resonators. In: Proceedings of IEEE MEMS, pp 9–14

Casset F, Durand C, Dedieu S, Carpentier JF, Gonchond JP, Ancey P, Robert P (2009) 3D multi-frequency MEMS electromechanical resonator design. In: Proceedings of EuroSimE, pp 1–5

Chamanian S, Bahrami M, Zangabad RP, Khodaei M, Zarbakhsh P (2012) Wideband capacitive energy harvester based on mechanical frequency-up conversion. In: Proceedings of IEEE SAS, pp 1–4

Chandrahalim H, Bhave SA (2008) Digitally-tunable mems filter using mechanically-coupled resonator array. In: Proceedings of IEEE MEMS, pp 1020–1023

Chidambaram N, Mazzalai A, Muralt P (2012) Comparison of lead zirconate titanate (PZT) thin films for MEMS energy harvester with interdigitated and parallel plate electrodes. In: Proceedings of ISAF/ECAPD/PFM, pp 1–4

Chidambaram N, Mazzalai A, Balma D, Muralt P (2013) Comparison of lead zirconate titanate thin films for microelectromechanical energy harvester with interdigitated and parallel plate electrodes. IEEE Trans Ultrason Ferroelectr Freq Control 60:1564–1571

Collado A, Georgiadis A (2013) Conformal hybrid solar and electromagnetic (EM) energy harvesting rectenna. IEEE Trans Circuits Syst 60:2225–2234

Cugat O, Delamare J, Reyne G (2003) Magnetic micro-actuators and systems (MAGMAS). IEEE Trans Magn 39:3607–3612

Dargie W, Poellabauer C (2010) Fundamentals of wireless sensor networks: theory and practice. John Wiley and Sons, Hoboken

Dini M, Romani A, Filippi M, Bottarel V, Ricotti G, Tartagni M (2015) A nano-current power management ic for multiple

heterogeneous energy harvesting sources. IEEE Trans Power Electron. doi:10.1109/TPEL.2014.2379622

Erturk A, Inman DJ (2011) Piezoelectric energy harvesting. John Wiley and Sons, Hoboken

Ferrari M, Ferrari V, Guizzetti M, Marioli D, Taroni A (2008) Piezoelectric multifrequency energy converter for power harvesting in autonomous microsystems. Sens Actuators A: Phys 142:329–335 **(Elsevier)**

Fu JL, Nakano Y, Sorenson LD, Ayazi F (2012) Multi-axis AlN-on-silicon vibration energy harvester with integrated frequency-upconverting transducers. In: Proceedings of IEEE MEMS, pp 1269–1272

Galchev T, Aktakka EE, Najafi K (2012) A piezoelectric parametric frequency increased generator for harvesting low-frequency vibrations. IEEE JMEMS 21:1311–1320

Goldschmidtboeing F, Wischke M, Eichhorn C, Woias P (2009) Nonlinear effects in piezoelectric vibration harvesters with high coupling factors. In: Proceedings of PowerMEMS, pp 364–367

Hagiwara K, Goto M, Iguchi Y, Tajima T, Yasuno Y, Kodama H, Kidokoro K, Suzuki Y (2012) Electret charging method based on soft X-ray photoionization for MEMS transducers. IEEE Trans Dielectr Electr Insul 19:1291–1298

Hajati A, Bathurst SP, Lee HJ, Kim SG (2011) Design and fabrication of a nonlinear resonator for ultra wide-bandwidth energy harvesting applications. In: Proceedings of IEEE MEMS, pp 1301–1304

Halvorsen E (2012) Fundamental issues in nonlinear wide-band vibration energy harvesting. APS Phys Rev E 87:1–6

Iannacci J, Sordo G (2016) Up-scaled macro-device implementation of a MEMS wideband vibration piezoelectric energy harvester design concept. Springer Microsystem Technologies XX:1–13. doi:10.1007/s00542-015-2794-y

Iannacci J, Serra E, Di Criscienzo R, Sordo G, Gottardi M, Borrielli A, Bonaldi M, Kuenzig T, Schrag G, Pandraud G, Sarro PM (2014) Multi-modal vibration based MEMS energy harvesters for ultra-low power wireless functional nodes. Springer Microsyst Technol 20:627–640

IXYS Solar Cell Products (2015) http://www.ixysic.com/Products/SolarCell.htm. Accessed 14 May 2015

Janphuang P, Lockhart R, Briand D, de Rooij NF (2014) On the optimization and performances of a compact piezoelectric impact MEMS energy harvester. In: Proceedings of IEEE MEMS, pp 429–432

Kamierski TJ, Beeby S (2010) Energy harvesting systems: principles, modeling and applications. Springer, Berlin

Kim I-H, Jung H-J, Lee BM, Jang S-J (2011) Broadband energy-harvesting using a two degree-of-freedom vibrating body. Appl Phys Lett 98:1–3

Kutiš V, Dzuba J, Paulech J, Murín J, Lalinský T (2012) MEMS piezoelectric pressure sensor-modelling and simulation. Procedia Eng 48:338–345. doi:10.1016/j.proeng.2012.09.523 **(Elsevier)**

Kymissis J, Kendall C, Paradiso J, Gershenfeld N (1998) Parasitic power harvesting in shoes. In: Proceedings of ISWC, pp 132–139

Lee BS, Wu WJ, Shih W-P, Vasic D, Costa F (2007) P2E−3 power harvesting using piezoelectric MEMS generator with interdigital electrodes. In: Proceedings of IEEE Ultrasonics Symposium, pp 1598–1601

Liu SW, Lye SW, Miao JM (2012) Sandwich structured electrostatic/electrets parallel-plate power generator for low acceleration and low frequency vibration energy harvesting. In: Proceedings of IEEE MEMS, pp 1277–1280

Mayrhofer PM, Euchner H, Bittner A, Schmid U (2015) Circular test structure for the determination of piezoelectric constants of ScxAl1−xN thin films applying laser doppler vibrometry and FEM simulations. Sens Actuators A: Phys 222:301–308 **(Elsevier)**

Miki S, Fujita T, Kotoge T, Jiang YG, Uehara M, Kanda K, Higuchi K, Maenaka K (2012) Electromagnetic energy harvester by using buried NdFeB. In: Proceedings of IEEE MEMS, pp 1221–1224

Ou Q, Chen X, Gutschmidt S, Wood A, Leigh N (2010) A two-mass cantilever beam model for vibration energy harvesting applications. In: Proceedings of IEEE Conference on Automation Science and Engineering (CASE), pp 301–306

Percy S, Knight C, McGarry S, Post A, Moore T, Cavanagh K (2014) Thermal energy harvesting for application at MEMS scale. Springer, Berlin

Popovic Z, Falkenstein EA, Costinett D, Zane R (2013) Low-power far-field wireless powering for wireless sensors. Proceedings of IEEE 101:1397–1407

Prabha RD, Rincon-Mora GA, Kim S (2011) Harvesting circuits for miniaturized photovoltaic cells. In: IEEE ISCAS International Symposium, pp 309–312

Qi S, Shuttleworth R, Oyadiji SO, Wright J (2010) Design of a multiresonant beam for broadband piezoelectric energy harvesting. IOP smart materials and structures 19:1–10

Romani A, Paganelli RP, Sangiorgi E, Tartagni M (2013) Joint modeling of piezoelectric transducers and power conversion circuits for energy harvesting applications. IEEE Sens J 13:916–925

Roundy S, Wright PK, Rabaey JM (2004) Energy scavenging for wireless sensor networks: with special focus on vibrations. Kluwer Academic Publishers, Dordrecht

Sanchez-Rojas JL, Hernando J, Donoso A, Bellido JC, Manzaneque T, Ababneh A, Seidel H, Schmid U (2010) Modal optimization and filtering in piezoelectric microplate resonators. J Micromech Microeng 20:1–7

Schneider M, Bittner A, Patocka F, Stöger-Pollach M, Halwax E, Schmid U (2012) Impact of the surface-near silicon substrate properties on the microstructure of sputter-deposited AlN thin films. Appl Phys Lett 101:1–3

Schneider M, Bittner A, Schmid U (2014) Thickness dependence of Young's modulus and residual stress of sputtered aluminum nitride thin films. Appl Phys Lett 105:1–4

Shahruz SM (2006) Design of mechanical band-pass filters for energy scavenging. J Sound Vib 292:987–998

Suzuki M, Matsushita N, Hirata T, Yoneya R, Onishi J, Wada T, Takahashi T, Nishida T, Yoshikawa Y, Aoyagi S (2011) Fabrication of highly dielectric nano-BaTiO3/epoxy-resin composite plate having trenches by mold casting and its application to capacitive energy harvesting. In:Proceedings of IEEE Transducers, pp 2642–2645

Tao K, Ding G, Wang P, Yang Z, Wang Y (2012) Fully integrated micro electromagnetic vibration energy harvesters with micro-patterning of bonded magnets. In: Proceedings of IEEE MEMS, pp 1237–1240

Todorov G, Valtchev S, Todorov T, Ivanov I, Klaassens B (2011) Tuning techniques for kinetic MEMS energy harvesters. In: Proceedings of IEEE INTELEC, pp 1–6

Uckelmann D, Harrison M, Michahelles F (eds) (2011) Architecting the internet of things. Springer, Berlin

Vasseur J-P, Dunkels A (2010) Interconnecting smart objects with IP: the next internet. Morgan Kaufmann Publishers, Burlington

Vullers RJM, Schaijk RV, Visser HJ, Penders J, Hoof CV (2010) Energy harvesting for autonomous wireless sensor networks. IEEE Solid-State Circuits Mag 2:29–38

Xue H, Hu Y, Wang Q-M (2008) Broadband piezoelectric energy harvesting devices using multiple bimorphs with different operating frequencies. IEEE Trans Ultrason Ferroelectr Freq Control 55:2104–2108

Zhu D (2011) Vibration energy harvesting: machinery vibration, human movement and flow induced vibration, in sustainable energy harvesting technologies—past present and future. InTech, Rijeka

Zhu M, Worthington E, Njuguna J (2009) Coupled piezoelectric-circuit FEA to study influence of a resistive load on power output of piezoelectric energy devices. Proc SPIE Smart Sens Actuators, MEMS IV 7326:1–12

Zorlu O, Topal ET, Külah H (2011) A vibration-based electromagnetic energy harvester using mechanical frequency up-conversion method. IEEE Sens J 11:481–488

Zukauskaite A, Wingqvist G, Palisaitis J, Jensen J, Persson Per OÅ, Matloub R, Muralt P, Kim Y, Birch J, Hultman L (2012) Microstructure and dielectric properties of piezoelectric magnetron sputtered w ScxAl1 xN thin films. J Appl Phys 111:1–7